Journal of
MATERIALS RESEARCH

Role of matrix microstructure in the ultrasonic characterization of fiber-reinforced metal matrix composites

S. Krishnamurthy
USAF Materials Directorate, Wright Laboratory, WL/MLLM/UES, Wright-Patterson AFB, Ohio 45433–7817

T. E. Matikas and P. Karpur
USAF Materials Directorate, Wright Laboratory, WL/MLLP/UDRI, Wright-Patterson AFB, Ohio 45433–7817

(Received 14 March 1996; accepted 1 November 1996)

This work deals with the application of ultrasonic nondestructive evaluation for characterizing fiber-reinforced metal matrix composites. The method involved the use of a recently developed technique in which the fiber reinforcement acts as a reflector to incident ultrasonic shear waves. Single fiber and multifiber, single ply composites consisting of SiC fibers in several titanium alloy matrices were investigated. The ultrasonic images obtained were correlated with the results of metallographic characterization of the composites. The results showed that the ultrasonic response of the metal matrix composites is significantly influenced by the microstructure of the matrix through which the incident wave traverses. The general effects of matrix on ultrasonic wave propagation are reviewed, and the ultrasonic signals obtained from various SiC fiber-reinforced titanium alloy composites are discussed in terms of the scattering effects of matrix microstructure.

I. INTRODUCTION

There are numerous studies dealing with the application of nondestructive evaluation (NDE) techniques for investigating fiber-reinforced metal matrix composites (MMC's). In particular, ultrasonic NDE techniques have been used in the past for determining the distribution of reinforcements and detecting *macroscopic* defects such as ply delaminations and nonuniform fiber spacing, arising from either missing fibers or displacement of fibers during fabrication of composite panels.[1,2] Recent work has demonstrated that ultrasonic NDE is an equally valuable technique for detecting *microscopic* defects arising during the processing of continuously reinforced MMC's, and that it can be reliably used to minimize the number of iterations required for optimization of the consolidation process.[3] Further, it has also been shown that ultrasonic NDE can serve as a powerful tool for studying important damage evolution phenomena in fiber-reinforced MMC's, including fiber fracture and fiber/matrix interfacial debonding.[4,5] However, when ultrasonic waves are used to evaluate a composite with a polycrystalline matrix, the waves propagating in the matrix will be scattered by the grains, and the ultrasonic evaluation of the material will be affected by the resulting noise.

Therefore, the objective of the present work is to study the influence of matrix alloy microstructure on ultrasonic wave propagation and its effects in evaluating the aforementioned damage evolution phenomena in MMC's. The role of grain boundaries is of particular importance since engineering alloys which are being considered for MMC matrix applications are polycrystalline in nature. When such materials consist of fine, single phase equiaxed grains with no preferred orientation, they may be treated as homogeneous and isotropic in many applications involving ultrasonic nondestructive evaluation because the ultrasonic wavelengths are generally orders of magnitude larger than the grain size. However, the matrix alloy microstructures that are commonly encountered in practice may consist of two or more phases with nonequiaxed morphologies and preferred orientation. Depending on their size and morphology, these microstructural features can change the direction of the ultrasonic wave group velocity, thereby significantly affecting the ultrasonic wave propagation.

This paper illustrates the influence of matrix on ultrasonic wave propagation in several Ti alloy/SiC fiber composites using the ultrasonic shear wave back-reflectivity (SBR) technique which was developed for studying the fiber/matrix interfacial characteristics.[3,4] First, the theoretical aspects of scattering of ultrasonic waves by a polycrystalline medium will be presented. This will be followed by the experimental work dealing with the ultrasonic characterization of SiC fiber-reinforced titanium alloy composites with a variety of matrix microstructures.

II. SCATTERING OF ULTRASONIC WAVES IN A MATERIAL

An ultrasonic pulse being transmitted by a transducer can be considered as a superposition of many sinusoids and can be represented by the Fourier integral:

$$u(x, t) = \int_{-\infty}^{+\infty} A(\kappa) e^{-i[\kappa x - \omega(\kappa) t + \varphi]} \, d\kappa \,, \qquad (1)$$

where κ is the wave number, φ is the phase, ω is the angular frequency, x is the spatial coordinate, and t is the time. It should be noted that although the integration is from $-\infty$ to $+\infty$, only some of the amplitudes, $A(\kappa)$, will be nonzero subject to the bandwidth of the transducer.

When a wave pulse defined by (1) propagates through a distance x_0, the effect of the propagation is equivalent to the pulse passing through a linear, time invariant filter with a frequency response given by

$$H(\omega) = e^{-i\kappa x_0} \,.$$

Hence, when a pulse defined by (1) is reflected by a plane reflector (located perpendicular to the direction of propagation and in an ideal noiseless and nonattenuative medium) at a distance $x_0/2$ and further propagates back to the receiver, the received signal is given by

$$r(x, t) = \int_{-\infty}^{+\infty} A(\kappa) e^{-i[\kappa x - \omega(\kappa) t + \varphi]} e^{-i(\kappa x_0)} d\kappa \,. \qquad (2)$$

The right-hand side of (2) is the same as the transmitted signal except for a phase lag introduced due to the wave propagation (diffraction and attenuation effects are ignored). However, when strong scatterers are present in the material in which the wave pulse is propagating, the scatterers contribute to a portion of the amplitude being sensed by the receiver. Thus, the received wave pulse, in the presence of scatterers, is defined by the following equation[6,7]:

$$\bar{r}(x, t) = \int_{-\infty}^{+\infty} A(\kappa) e^{-i[\kappa x - \omega(\kappa) t + \varphi]} e^{-i(\kappa x_0)} d\kappa + \int_{-\infty}^{+\infty} A(\kappa) e^{-i[\kappa x - \omega(\kappa) t + \varphi]} e^{-i(\kappa x_0)} s(\kappa) d\kappa \,, \qquad (3)$$

where $s(\kappa) = \oint e^{-i\phi_{\kappa,n}} dn$ represents the integration over all the scatterers present in the resolution volume of the pulse.

It is clear from Eq. (3) above that the first term on the right-hand side is the transmitted signal itself except for a change in the phase delay which is a direct function of the ratio of the distance of propagation and wavelength or the product of the propagation distance and the wave number. However, the second term on the right-hand side of this equation has a random phase $(\phi_{k,n})$ component. The randomness in the phase is introduced because the phase of the scattered wave component will be a function of the wave number and the position of the scatterer within the resolution volume. Although Eq. (3) shows only the ultrasonic attenuation due to grain scattering, there are additional acoustic energy losses such as geometrical losses due to beam spreading and wave attenuation caused by absorption. Geometrical losses are neglected here because, as will be discussed later, this is a comparative study of various specimens with different matrix microstructures, but with identical testing geometry and similar sound velocity for all the specimens. However, absorption effects are considered here and Eqs. (1) to (3) can be modified to represent the amplitude of the elastic stress wave traveling in the material to a general form as shown below:

$$A = A_{\text{att}} \cdot A_{\text{prop}} \,, \qquad (4)$$

where A_{att} is the attenuated amplitude due to scattering and A_{prop} is the propagation term given by

$$A_{\text{att}} = A_0 e^{-\alpha(f)x} \qquad (5)$$

and

$$A_{\text{prop}} = \sin(\beta x - \omega t) \,, \qquad (6)$$

where A_0 is the initial amplitude, x is the distance over which the wave front has traveled, $\alpha(f)$ is the attenuation coefficient which is a function of the frequency $f = \omega/2\pi$ of ultrasound, $\beta = 2\pi f/v$ is a propagation constant, and v is the phase velocity. The attenuation coefficient of a polycrystalline material is defined by

$$\alpha(f) = \alpha_a(f) + \alpha_s(f) \,, \qquad (7)$$

where α_a is the absorption coefficient and α_s is the grain scattering coefficient due to energy dispersion of the traveling waves.[8] The velocity of wave propagation is determined by the elastic moduli, which again depends on the orientation of the grains. If a preferred grain orientation exists, the medium can become elastically anisotropic as a whole, so that the velocity is a function of the direction of propagation.

The scattering is dependent on the type, size, and orientation of the grains as well as the mode of incident waves. The grain scattering problem has been solved by Lifshitz *et al.* for an isotropic, equiaxed, homogeneous polycrystalline material.[9] Three distinct domains of attenuation caused by grain scattering exist: (a) Rayleigh domain when the wavelength $\lambda > 2\pi D_g$, (b) stochastic domain when $\lambda \approx 2\pi D_g$, and (c) diffusion domain when $\lambda < 2\pi D_g$, where D_g is the average grain diameter with an approximation of spherical grains. The analytical solutions of scattering coefficients for each of these cases may be found in the literature. For example, Merkulov obtained the general solutions of both Rayleigh and diffusion scattering for the special

cases of cubic and hexagonal metals.[10] An equivalent theoretical analysis was performed by Bhatia and Moore for Rayleigh scattering in the case of orthorhombic materials.[11] In general, the attenuation due to grain scattering for all the different cases can be written in the form

$$\alpha(\lambda) = a_1/\lambda + a_2 {D_g}^3/\lambda^4, \qquad \text{when } \lambda > 2\pi D_g, \tag{8a}$$

$$\alpha(\lambda) = b_1/\lambda + b_2 D_g/\lambda^2, \qquad \text{when } \lambda \approx 2\pi D_g, \tag{8b}$$

$$\alpha(\lambda) = c_1/\lambda + c_2/\lambda^2 + c_3/D_g, \qquad \text{when } \lambda < 2\pi D_g, \tag{8c}$$

where a_1, b_1, c_1, and c_2 are absorption coefficients, and a_2, b_2, and c_3 are scattering coefficients. Thus, from (8a), (8b), and (8c), it is clear that

(i) when $\lambda > 2\pi D_g$ (Rayleigh scattering),

$$\alpha_s(\lambda) = C_1 {D_g}^3/\lambda^4, \tag{9a}$$

(ii) when $\lambda \approx 2\pi D_g$ (stochastic scattering),

$$\alpha_s(\lambda) = C_2 D_g/\lambda^2, \tag{9b}$$

and

(iii) when $\lambda < 2\pi D_g$ (diffusion scattering),

$$\alpha_s(\lambda) = C_3/D_g \tag{9c}$$

where C_1, C_2, and C_3 are constants.

Hence, the degree of scattering is a function of both the wavelength, λ, of the incident ultrasonic waves and the average grain dimension D_g. It should be noted that the relationships (9a) to (9c) are valid only if the grain shape can be approximated as spherical (equiaxed). Also, the above analysis considers grain boundary scattering in single phase materials. In the case of multiphase materials, the impedance mismatch between the constituents of the microstructure is of great importance. This impedance mismatch clearly affects the amounts of scattering coefficients [*C*1, *C*2, and *C*3 in Eqs. 9(a), 9(b), and 9(c), respectively].

In the case of columnar grains, the structure does not conform to the model of spherical grains assumed for equiaxed grains, and therefore, Eqs. (9a) to (9c) are no longer valid. Columnar grains, because of the waveguide phenomenon, might cause different modes of "guided-waves" to propagate in the test material. Propagation of higher modes is dependent on the frequency and the cross-sectional dimension of the columnar grains. When the frequency is varied over a range, new modes of wave propagation are induced in the columnar material, depending on the ratio of the cross-sectional dimension and the wavelength. Mathematical relations are available for circular and rectangular ducts from which the cross-sectional dimension of the duct can be calculated as a function of the wavelength.[12,13] However, since columnar grains generally have irregular cross-sectional shape, the analytical expressions are only approximations of the relationship between the wavelength and the average cross-sectional dimension of the grains.

Columnar grains can have a major effect on wave propagation, especially when the elongated direction of the grains does not coincide with the direction of wave transmission. Under such conditions, the direction of propagation of the wave front (group velocity vector) will be modulated, resulting in the skewing of the acoustic beam. As a result, the transmitted ultrasonic energy might not reach the intended target in the material, thereby producing a distorted image. One form of distortion is the production of a patchy image wherein the acoustic beam reaches the intended target at some locations and misses the target in others due to inhomogeneities in the microstructure. A similar effect may be evident in the case of textured materials, wherein the preferred orientation of grains may change the scattering of elastic waves traveling in the material. The basic mechanism of change in scattering is due to the reduced impedance to the acoustic wave front, when the direction of wave propagation coincides with the preferred orientation of the grains. When both columnar grains and preferred orientation are present, the effect of beam distortion may be further accentuated.

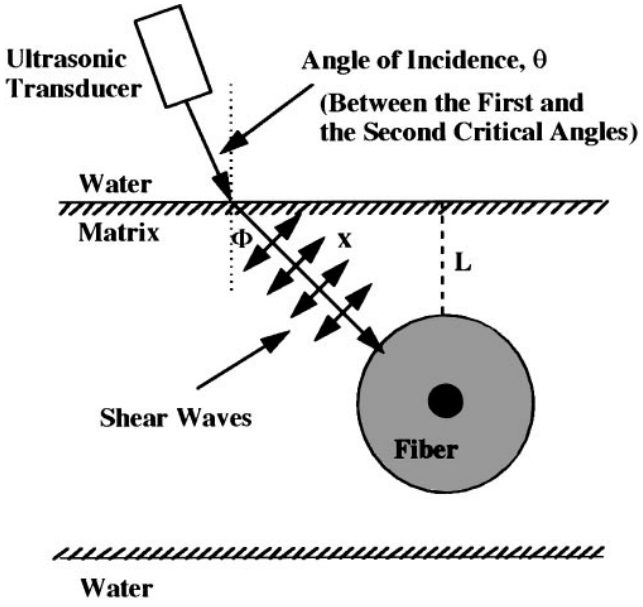

FIG. 1. Schematic diagram of the transverse section of a continuously reinforced composite showing shear wave interrogation of a ceramic fiber embedded in a metal matrix. Angle of incidence $\theta = 24°$; refraction angle $\Phi = 60°$ (Ti–6Al–4V matrix); distance of the fiber position from the upper specimen surface $L = 1$ mm; traveling distance of shear waves $x = 2$ mm.

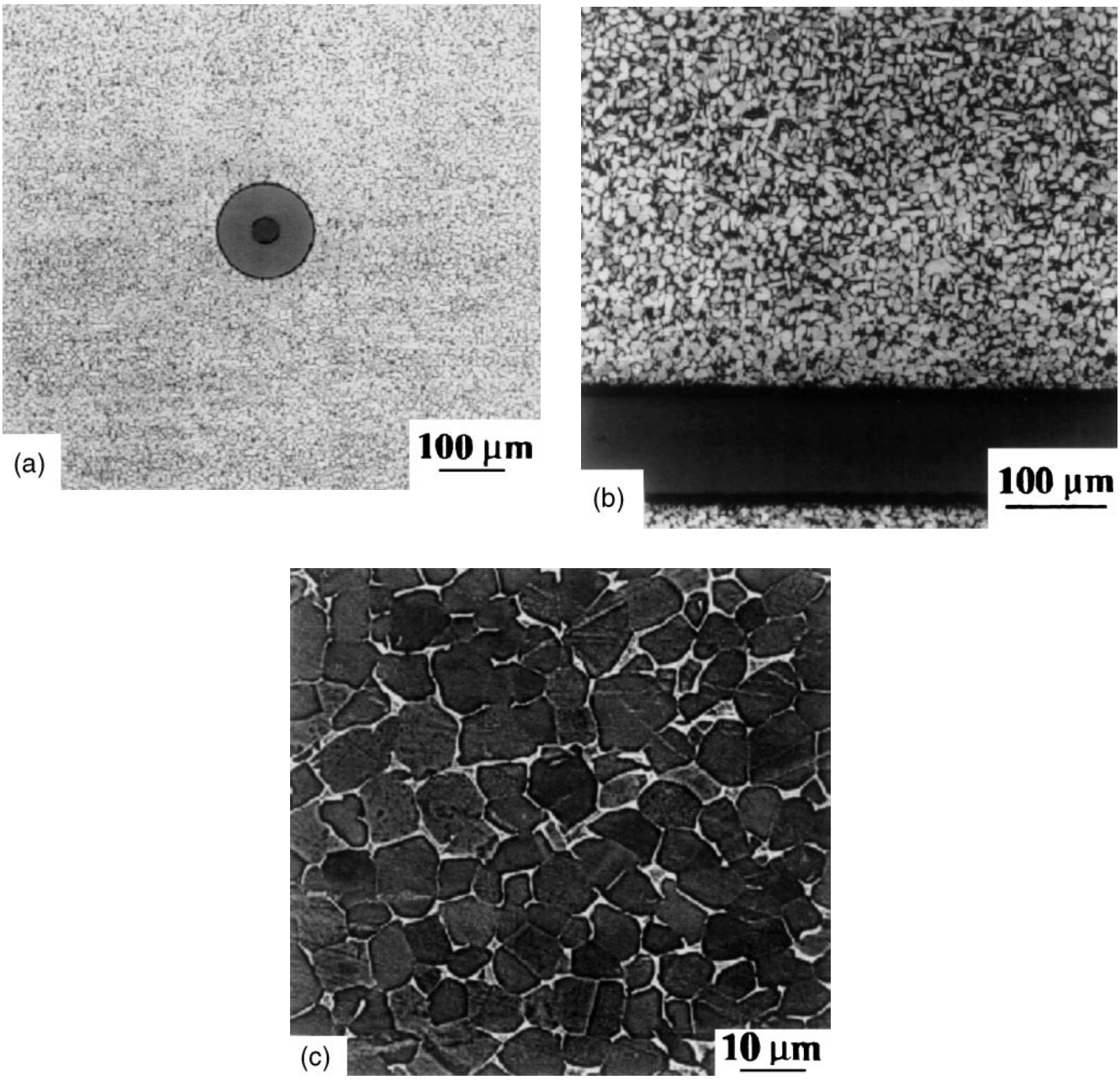

FIG. 2. (a, b) Optical micrographs and (c) back-scattered electron SEM micrograph showing the microstructure of a Ti–6Al–4V/SiC single fiber composite which was consolidated in the sub-transus region. (a) Transverse section, (b) longitudinal section, and (c) higher magnification image of matrix.

III. EXPERIMENTAL

A. Matrix alloys

The following titanium alloys were used for processing the composites studied in this work: Ti–6Al–4V, Ti–14Al–21Nb, Ti–15Mo–2.7Nb–3Al–0.2Si (TIMETAL 21S), and Ti–12Al–41Nb (compositions in wt. %). Among these, the Ti–12Al–41Nb alloy, corresponding to Ti–24Al–24Nb in at. %, belongs to the class of "orthorhombic" titanium aluminide matrix alloys which are being considered for composite applications at moderately elevated temperatures. The other alloys that are listed here have been candidates for matrix applications at relatively lower temperatures.

B. Fabrication of composite specimens

Model single fiber and single ply composite samples consisting of SCS-6 SiC fibers in the various titanium alloy matrices were fabricated by diffusion bonding of

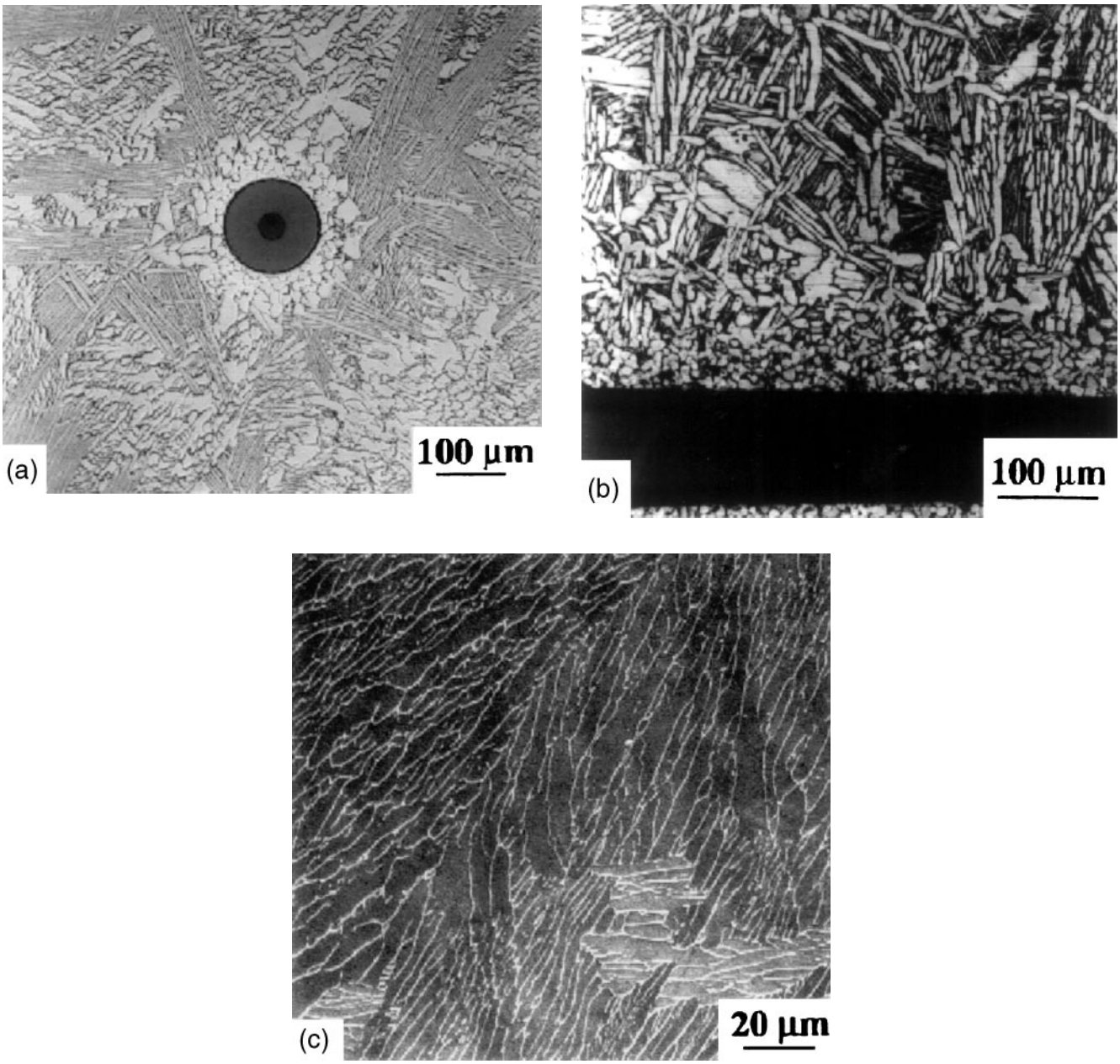

FIG. 3. (a, b) Optical micrographs and (c) SEM micrograph showing the microstructure of a Ti–6Al–4V/SiC single fiber composite which was consolidated in the supra-transus region. (a) Transverse section, (b) longitudinal section, and (c) higher magnification image of matrix.

the reinforcement placed between two titanium alloy sheets using vacuum hot pressing and/or hot isostatic pressing (HIP'ing). The Ti–14Al–21Nb/SCS-6 and Ti–12Al–41Nb/SCS-6 composites were consolidated in the two-phase regions below the beta-transus temperature using a two-step process involving vacuum hot pressing at 925 °C under a pressure of 5.5 MPa for 30 min followed by HIP'ing at 1010 °C under 100 MPa pressure for 2 h. The TIMETAL 21S/SCS-6 composite was processed within the beta phase field by hot pressing at 925 °C for 1 h under a pressure of 10 MPa. In the case of the Ti–6Al–4V alloy, with a β-transus temperature of ~995 °C, two different types of composite specimens were fabricated by performing consolidation at either sub-transus or supra-transus regions. The sub-transus processing was carried out by HIP'ing at 950 °C for 2 h using a pressure of 100 MPa, while the supra-transus consolidation conditions were identical to those of the two-step processing outlined earlier. The consolidated composite panels were typically 2 mm thick with the single fiber or layer of fibers located at the midplane of the panels.

C. Ultrasonic imaging

The fiber embedded in the matrix material was ultrasonically imaged using shear wave interrogation. A schematic of the SBR method is shown in Fig. 1. Using this technique, a 25 MHz focused ultrasonic transducer (6.3 mm diameter, 12.7 mm focal length) was operated in pulse-echo mode. In order to image the embedded fibers, the wavelength of ultrasonic waves, λ, needed to be comparable to the diameter of the fibers (about 140 μm for the SCS-6 fibers). Therefore, the ultrasonic frequency, f, was chosen to be 25 MHz ($\lambda \approx$ 100–130 μm, depending on the shear wave velocity in the Ti matrix material). The shear wave velocities, c_S, in the different matrix alloys used in this study, were measured by time-of-flight technique and the corresponding wavelengths were calculated ($\lambda = c_S/f$). The ultrasonic wave front was incident on the specimen surface inclined to the vertical plane at an angle of either 18° or 24°. Both these angles lie between the first and the second critical angles, which are defined as the angles of incidence above which longitudinal and shear waves, respectively, will not propagate in the matrix material. As a result, only vertically polarized shear waves propagated in the matrix and were incident on the fiber/matrix interface (Fig. 1). For an angle of incidence $\theta = 24°$, the refraction angle in the matrix can be calculated by Snell's law and is $\Phi = 60°$ for Ti–6Al–4V. The distance, L, of the fiber position from the upper specimen surface was about 1 mm. Therefore, the shear wave traveling distance, x, was about 2 mm. All the different specimens used in this study had the same geometry. The image of the fiber was obtained by scanning the ultrasonic transducer along and across the fiber with an increment of 25 μm between signal acquisition points. At each point, the back-reflected ultrasound was software-gated[14] for imaging. Because of substantial mismatch in acoustic impedance (due to mismatch in elastic properties) between the Ti-based matrix and SiC fiber, there is a very strong back-reflected ultrasonic signal.

D. Metallography

In order to study the correlation between the ultrasonic image and the local microstructure, all the composite panels were cut normal to the fiber axis and also normal to the panel along the fiber axis to examine their transverse and longitudinal sections, respectively. It was important to characterize both these sections due to the following reasons: The transverse sections were useful for checking the consolidation of the composites and for determining the position of the fibers within the composite panel. On the other hand, the longitudinal sections were required to ascertain that the composite samples were free from damage such as fiber fracture and matrix cracking. These sections were metallographically polished and examined by optical and scanning electron microscopy (SEM) techniques.

IV. RESULTS AND DISCUSSION

A. MMC microstructures

1. Ti–6Al–4V/SCS-6 (Sub-transus processing)

Optical micrographs from the transverse and the longitudinal sections of this composite are shown in Figs. 2(a) and 2(b), respectively. These micrographs depict a fine equiaxed matrix microstructure in this composite panel. Figure 2(c) is an SEM back-scattered electron image taken at a higher magnification and shows equiaxed α phase grains (dark regions) forming the major part of this structure with a minor amount of β phase (bright regions) present at α grain boundaries. The grain size of the α phase was measured to be about 10 μm, and the average thickness of the β regions was <1 μm.

2. Ti–6Al–4V/SCS-6 (Supra-transus processing)

This material showed a typical β-transformed matrix composed of an ($\alpha + \beta$) two-phase "basket weave" microstructure (Fig. 3). Figure 3(c) is an SEM image from a "basket weave" region, indicating the high aspect ratio α plates and β ligaments formed in various directions. This elongated morphology was predominant throughout the composite panel except for a very small region of the matrix within $\sim$100 μm from the fiber as observed in Figs. 3(a) and 3(b). The matrix in this narrow region showed an equiaxed microstructure similar to that seen in Fig. 2 corresponding to sub-transus processing.

Figure 4 shows an optical micrograph from a transverse section of a Ti–6Al–4V/SCS-6 panel containing only three fibers which was also consolidated in the

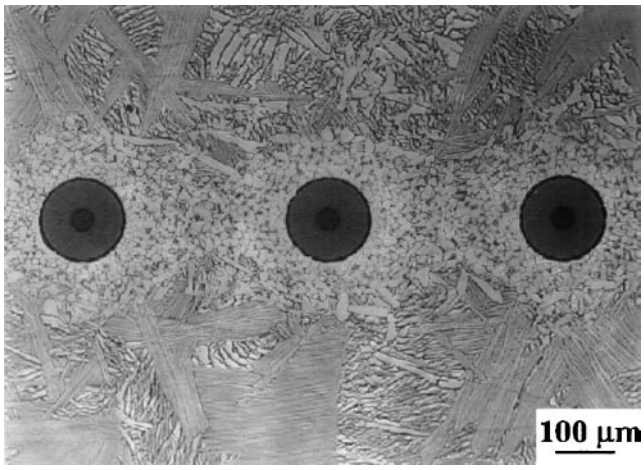

FIG. 4. Optical micrograph showing the matrix microstructure around three fibers in a Ti–6Al–4V/SiC single-ply composite which was consolidated in the supra-transus region.

supra-transus region. The matrix microstructure in this pane was very similar to that of the single-fiber case.

3. Ti–14Al–21Nb/SCS-6

The matrix in this composite was composed of a fine equiaxed ($\alpha_2 + \beta$) two-phase microstructure (Fig. 5). The α_2 phase, which formed a major part of this matrix, was equiaxed with a grain size in the range 8–10 μm. The β phase displayed irregular morphologies and formed in minor amounts at α_2 grain boundaries. This microstructure was similar to that of the Ti–6Al–4V matrix which was processed in the sub-transus range (Fig. 2).

4. TIMETAL 21S/SCS-6

Figure 6 shows the microstructure of this composite. The matrix of this composite consisted of β phase with an average grain size of ~70 μm. Some subgrain structure was also observed as indicated in Fig. 6(a).

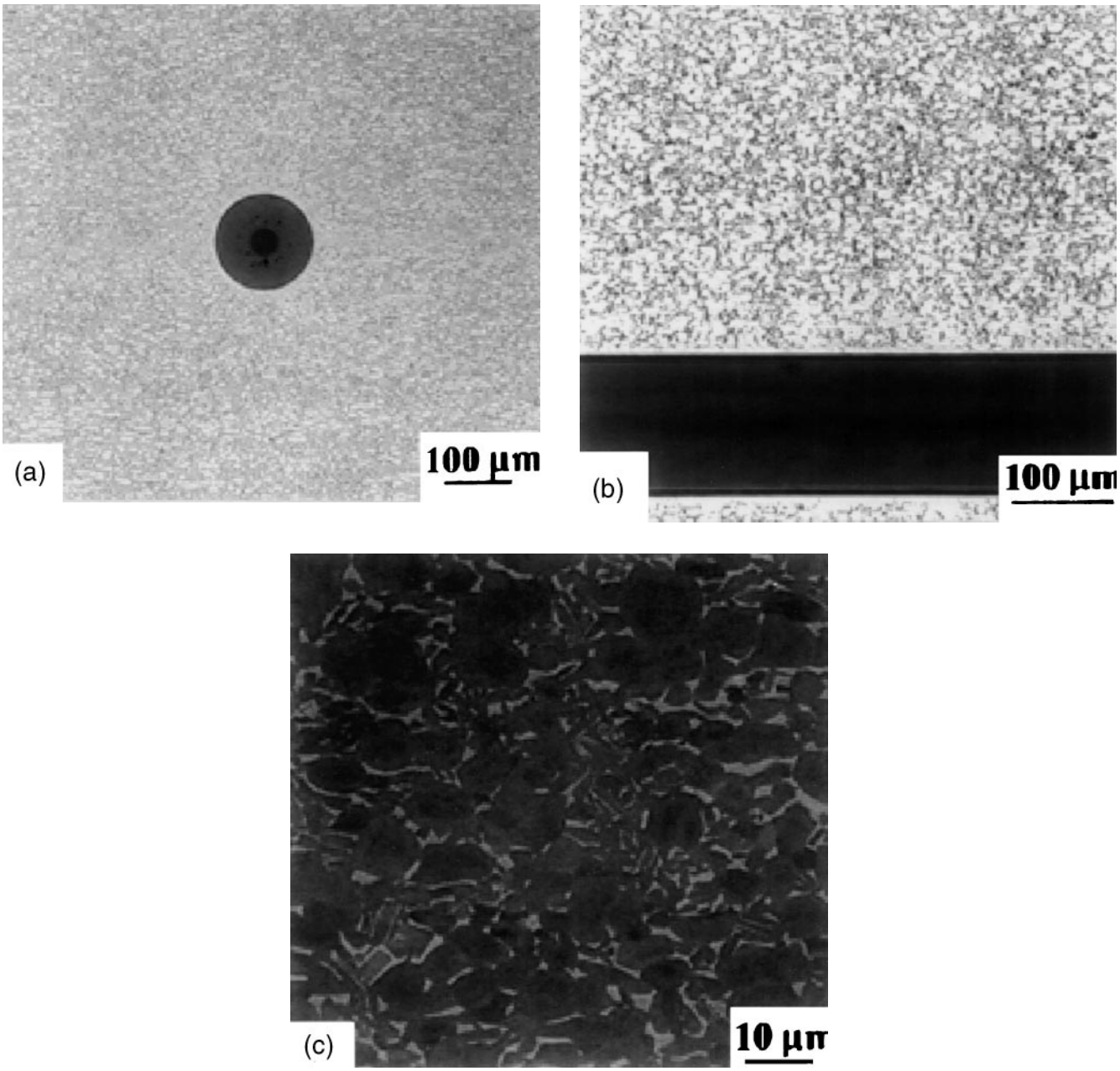

FIG. 5. (a, b) Optical micrographs and (c) SEM micrograph showing the microstructure of a Ti–14Al–21Nb/SiC single fiber composite. (a) Transverse section, (b) longitudinal section, and (c) higher magnification image of matrix.

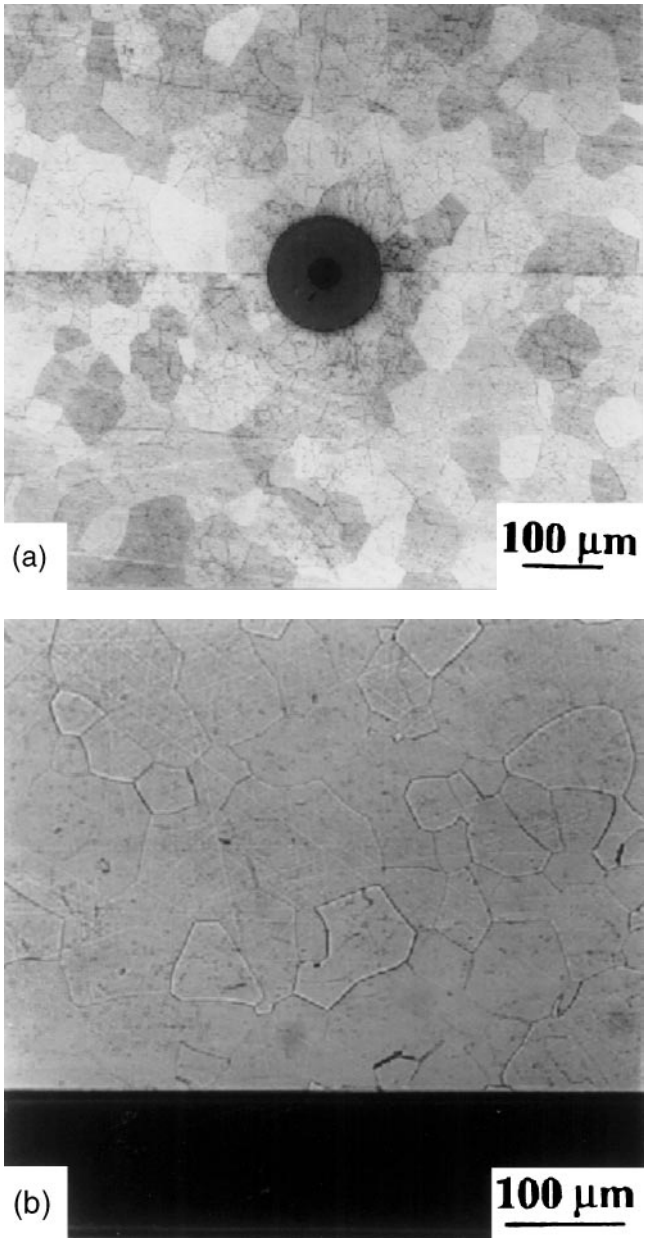

FIG. 6. Optical micrographs showing the microstructure of a TIMETAL 21S/SiC single fiber composite. (a) Transverse section and (b) longitudinal section.

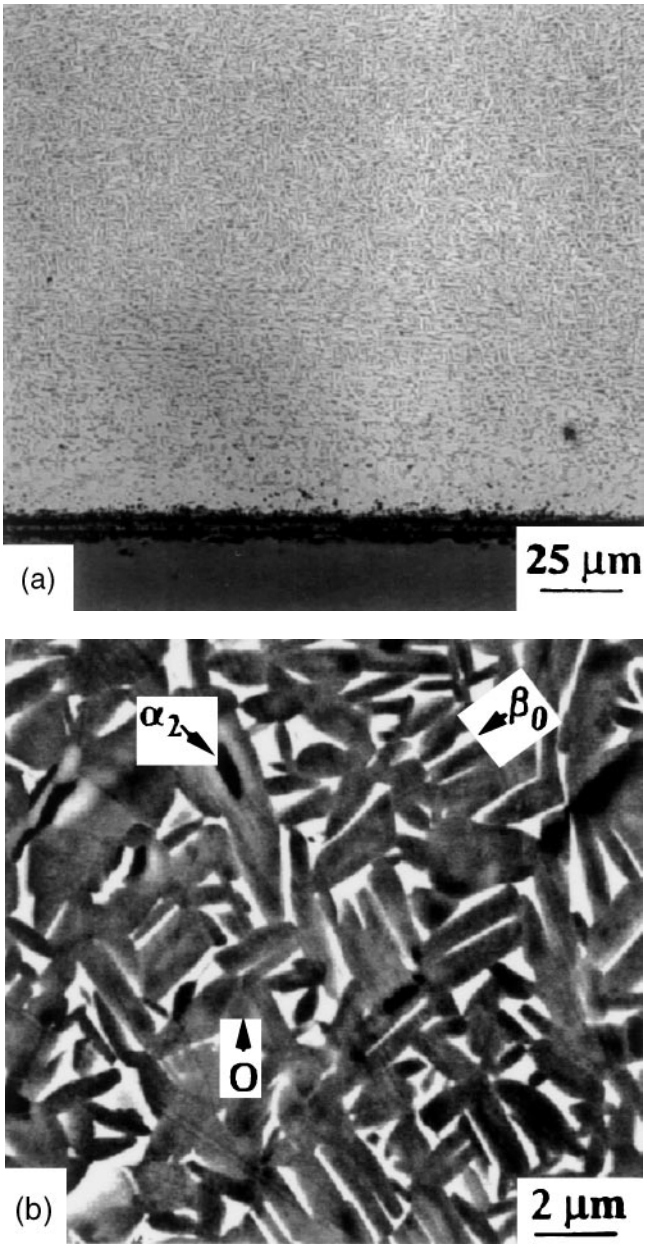

FIG. 7. (a) Optical micrograph and (b) back-scattered electron SEM micrograph showing the microstructure of a Ti–12Al–41Nb/SiC single fiber composite. (a) Longitudinal section and (b) higher magnification image of matrix.

5. Ti–12Al–41Nb/SCS-6

The microstructure of the matrix in this composite was considerably finer than that of the other matrices studied in this work. The matrix consisted of three phases, namely, orthorhombic (O), ordered beta (β_0), and α_2 which were distributed on a very fine scale as indicated by the arrows in Fig. 7. The orthorhombic phase, corresponding to the continuous gray regions in Fig. 7(b), formed the major part of this matrix. The mean grain intercept of the orthorhombic phase regions was measured to be 1 to 2 μm. The bright regions in Fig. 7(b) correspond to β_0 platelets which were a few microns in length and oriented in various directions.

Table I summarizes the various Ti-alloy matrix phases present, their morphology and average grain size of the relevant phases, along with the ultrasonic shear wave velocities and the corresponding wavelengths. The discussion about the ultrasonic images of SiC fiber(s) embedded in various matrices is based on the morphology of the matrix phases and the comparison

TABLE I. Different matrix alloy microstructural characteristics and the corresponding ultrasonic wave parameters.

Alloy composition (wt. %)	Matrix phases/morphology	D_g (μm) of major phase	C_s (m/s) (macroscopic)	λ (μm)
Ti–6Al–4V (i)	(α + β) equiaxed	10 (α)	3160	126
Ti–6Al–4V (ii)	(α + β) elongated	. . .	3160	126
Ti–14Al–21Nb	(α_2 + β) equiaxed	<10 (α_2)	3200	128
Ti–15Mo–2.7Nb–3Al–0.2Si (TIMETAL 21S)	β, equiaxed	70	2400	96
Ti–12Al–41Nb	(O + β_0 + α_2) platelets	. . .	3050	122

between grain size and ultrasonic wavelength for the frequency of shear waves used in this study (25 MHz).

It should be noted that in the case of multiphase alloys, the first matrix phase listed in Table I, second column, refers to the major phase in the microstructure. This major phase has a dominant effect on the ultrasonic wave propagation. Hence, in the case of the equiaxed microstructure, the ultrasonic wavelength is compared with the average size of the major phase. As can be observed from the table, the ultrasonic wavelength was much larger than the average grain size of the major phase.

B. Ultrasonic images

Figure 8 shows the ultrasonic images from the different composites studied in this work. The ultrasonic images were obtained by monitoring the shear acoustic waves back-reflected from the SiC fiber(s) embedded in the various metallic matrices.

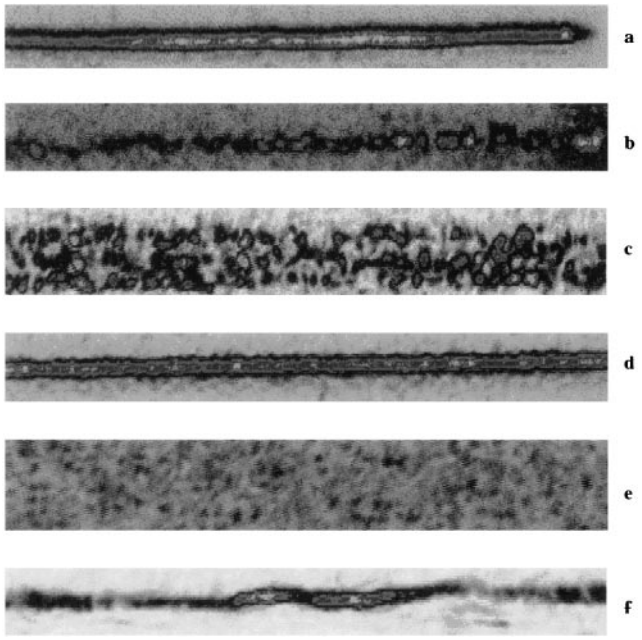

FIG. 8. SBR ultrasonic images from the various SiC fiber-reinforced, titanium-based composites corresponding to the matrix microstructures shown in Figs. 2–7, respectively; (a) Ti–6Al–4V/SiC single fiber composite processed in the sub-transus region, (b) Ti–6Al–4V/SiC single fiber composite processed in the supra-transus region, (c) Ti–6Al–4V/SiC single ply composite processed in the supra-transus region, (d) Ti–14Al–21Nb/SiC single fiber composite, (e) TIMETAL 21S/SiC single fiber composite, and (f) Ti–12Al–41Nb/SiC single fiber composite.

Figure 8(a) shows the image of a single-fiber Ti–6Al–4V/SCS-6 composite made with sub-transus processing (see Fig. 2). Since the matrix in this case is equiaxed and fine-grained ($D_g = 10$ μm), the wavelength, λ, is large compared to D_g. Therefore, the attenuation, $\alpha_s(\lambda)$, of the ultrasonic waves caused by grain scattering is in the Rayleigh domain, and is proportional to D_g^3/λ^4 [see Eq. 9(a)]. In this case, since $D_g/\lambda \ll 1$, $\alpha_s(\lambda)$ is negligible, and therefore, the ultrasonic image of the fiber is very clear.

Figure 8(b) shows the image of a single-fiber Ti–6Al–4V/SCS-6 composite made with supra-transus processing (see Fig. 3). Since the matrix in this case is elongated, guided waves are propagated in the material. For reasons given earlier in this paper, the ultrasonic waves transmitted in the matrix do not always reach the embedded reflector (fiber), thereby producing a patchy image of the fiber.

Figure 8(c) shows the image of a single-ply Ti–6Al–4V/SCS-6 composite made with supra-transus processing (see Fig. 4). The image shows only three of the fibers. The matrix in this case is again elongated; hence, guided waves are propagated in the material, and a patchy image of the three fibers is produced similar to the result obtained in Fig. 8(b).

Figure 8(d) shows the image of a single-fiber Ti–14Al–21Nb/SCS-6 composite (see Fig. 5). Since the matrix in this case is equiaxed and fine-grained ($D_g < 10$ μm), the wavelength $\lambda \gg D_g$. Therefore, the attenuation of the ultrasonic waves caused by grain scattering is in the Rayleigh domain and is negligible in value [see Eq. (9a)]. Hence, a very clear ultrasonic image of the fiber is obtained, similar to Fig. 8(a).

Figure 8(e) shows the image of a single-fiber Ti–15Mo–2.7Nb–3Al–0.2Si/SCS-6 composite (see Fig. 6). The matrix in this case is equiaxed, but the grain size is relatively large ($D_g = 70$ μm) and comparable to the wavelength $\lambda \approx D_g$. Therefore, the attenuation of the ultrasonic signal caused by grain scattering is in the stochastic domain and is proportional to D_g/λ^2 [see Eq. (9b)]. In this case, $\lambda \approx D_g$, and therefore, the attenuation of ultrasonic waves is proportional to

the frequency of interrogation: $\alpha_s(\lambda)$ is proportional to $1/\lambda$ or f. Since the imaging of the embedded fiber(s) required a relatively high frequency of interrogation (about 25 MHz), the back-reflected ultrasonic signal was completely attenuated, and it was impossible to image the fiber using the SBR technique. As discussed before, while waves with lower ultrasonic frequencies may propagate in the matrix with much lower attenuation, the corresponding wavelengths would be large compared to the fiber diameter, thereby precluding the imaging of the fiber.

Figure 8(f) shows the image of a single-fiber Ti–12Al–41Nb/SCS-6 composite (see Fig. 7). Since the matrix structure in this case contains a large number of β_0 platelets, preferential wave propagation (wave-microguide effect) occurs on a microscale in the material. Because of the fine nature of the platelets, the ultrasonic wave front is distorted when it reaches the embedded fiber. Hence, the resulting image of the fiber appears distorted.

V. SUMMARY

This paper deals with the effect of matrix microstructure on the ultrasonic evaluation of fiber reinforced metallic composite materials. The results have provided an insight into the applicability of the ultrasonic shear wave back-reflectivity (SBR) technique to study MMC's with several matrix microstructures. The present work shows that the ultrasonic image is greatly influenced by the magnitude of ultrasonic wavelength (or frequency) relative to the scale of the microstructural unit or grain size of matrix phases through which the ultrasonic wave propagates. The morphology of the matrix phases has also been shown to have a dominant effect. It is evident that the scattering of ultrasound by the matrix material can affect the imaging of embedded fibers leading to image distortion or complete loss of ultrasonic signal. These effects are important while applying ultrasonic techniques for the evaluation of defects, fiber fractures, or fiber/matrix interfacial debonding in metal matrix composites.

ACKNOWLEDGMENTS

This research was performed at the Air Force Wright Laboratory, Materials Directorate, under AF Contracts F33615-91-C-5663 (SK) and F33615-94-C-5213 (TEM and PK). The authors would like to thank Dr. D. B. Miracle, Wright Laboratory, Materials Directorate, for reviewing the manuscript and helpful comments. The technical assistance of W. A. Houston of UES, Inc., in metallographic specimen preparation is also acknowledged.

REFERENCES

1. W. S. Johnson, J. Composites Technology & Research **11**, 31–34 (1989).
2. P. K. Liaw, R. E. Shannon, W. G. Clark, W. C. Harrigan, H. Jeong, and D. K. Hsu, JOM **44**, 36–40 (1992).
3. S. Krishnamurthy, T. E. Matikas, P. Karpur, and D. B. Miracle, Composites Sci. Technol. **54**, 161–168 (1995).
4. P. Karpur, T. E. Matikas, and S. Krishnamurthy, *Am. Soc. for Composites Seventh Technical Conference on Composite Materials, Mechanics and Processing,* (Technomic Publishing Inc., Pennsylvania State University, University Park, PA, 1992), Vol. 1, pp. 420–427.
5. T. E. Matikas, P. Karpur, N. J. Pagano, S. Hu and L. Shaw, *21st Annual Review of Progress in Quantitative Nondestructive Evaluation,* edited by D. O. Thompson, and D. E. Chimenti (Plenum, Snowmass Village, CO, 1994), Vol. 14B, pp. 1327–1332.
6. E. A. Robinson and M. T. Silvia, *Digital Foundations of Time Series Analysis: Wave Equation-Processing* (Holden-Day, Inc., 1981), Vol. 2.
7. P. Karpur, J. Non-Destructive Evaluation, Indian Society for Non-Destructive Testing **10** (1), 19–28 (1990).
8. E. P. Papadakis, *Physical Acoustics,* edited by W. P. Mason (Academic Press, New York, 1968), Vol. IV-B, pp. 269–328.
9. E. M. Lifshitz and G. D. Parkhomovskii, Zh. Eksperim. i Teoret. Fiz. **20**, 175–182 (1950).
10. L. G. Merkulov, Sov. Phys.–Tech. Phys. (English Transl.) **1**, 59–69 (1956).
11. A. B. Bhatia and R. A. Moore, J. Acoust. Soc. Am. **31**, 1140–1142 (1959).
12. P. M. Morse and K. V. Ingard, *Theoretical Acoustics* (McGraw-Hill Book Co., New York, 1968).
13. T. R. Meeker and A. H. Meitzler, *Physical Acoustics,* edited by W. P. Mason (Academic Press, New York, 1964), Vol. I-A, pp. 111–167.
14. C. F. Buynak, T. J. Moran, and R. W. Martin, Mater. Eval. **47**, 438–447 (1989).